

# Model for Basin Effects on Long-Period Response Spectra in Southern California

Steven M. Day,<sup>a)</sup> Robert Graves,<sup>b)</sup> Jacobo Bielak,<sup>c)</sup> Douglas Dreger,<sup>d)</sup>  
Shawn Larsen,<sup>e)</sup> Kim B. Olsen,<sup>a)</sup> Arben Pitarka,<sup>b)</sup> and  
Leonardo Ramirez-Guzman<sup>c)</sup>

We propose a model for the effect of sedimentary basin depth on long-period response spectra. The model is based on the analysis of 3-D numerical simulations (finite element and finite difference) of long-period (2–10 s) ground motions for a suite of sixty scenario earthquakes (Mw 6.3 to Mw 7.1) within the Los Angeles basin region. We find depth to the 1.5 km/s *S*-wave velocity isosurface to be a suitable predictor variable, and also present alternative versions of the model based on depths to the 1.0 and 2.5 km/s isosurfaces. The resulting mean basin-depth effect is period dependent, and both smoother (as a function of period and depth) and higher in amplitude than predictions from local 1-D models. The main requirement for the use of the results in construction of attenuation relationships is determining the extent to which the basin effect, as defined and quantified in this study, is already accounted for implicitly in existing attenuation relationships, through (1) departures of the average “rock” site from our idealized reference model, and (2) correlation of basin depth with other predictor variables (such as  $V_{s30}$ ). [DOI: 10.1193/1.2857545]

## INTRODUCTION

The entrapment and amplification of seismic waves by deep sedimentary basins produces important effects on seismic wavefields (e.g., King and Tucker 1984; Field 1996; Joyner 2000) and response spectra (e.g., Trifunac and Lee 1978; Campbell 1997; Field 2000; Choi et al. 2005). These amplification effects are three-dimensional, and they are difficult to quantify empirically with currently available strong motion data, especially for periods longer than 1 second and sedimentary thicknesses exceeding 3 km or so (Campbell and Bozorgnia 2008).

Numerical simulations of earthquake ground motion have the potential to complement empirical methods for the study of basin effects. A number of studies have simulated 3-D seismic wave propagation in regional geological models that include basin

---

<sup>a)</sup> Department of Geological Sciences, San Diego State University, San Diego CA 92182

<sup>b)</sup> URS Corporation, 566 El Dorado Street, Pasadena CA 91101

<sup>c)</sup> Department of Civil and Environmental Engineering, Carnegie-Mellon University, Pittsburgh PA 15213

<sup>d)</sup> Berkeley Seismological Laboratory, University of California, Berkeley, Berkeley CA 94720

<sup>e)</sup> Lawrence Livermore National Laboratory, Livermore CA 94550

structure (e.g., Frankel and Vidale 1992; Olsen 1994; Olsen et al. 1995; Pitarka et al. 1998; Graves et al. 1998). Moreover, the recent availability of comprehensive 3-D earth models for southern California (e.g., Magistrale et al. 2000; Kohler et al. 2003; Suss and Shaw 2003) has substantially advanced our capability for simulating ground motion in that region (e.g., Olsen 2000; Komatitsch et al. 2004; Olsen et al. 2006). In the current study, we simulate ground motions for a set of earthquake scenarios for southern California, in an effort to quantify the effects of sedimentary basins on long-period ( $\geq \sim 2$  seconds) response spectra. The study employs both finite element (FE) and finite difference (FD) methods to compute ground motion from propagating earthquake sources, using the Southern California Earthquake Center (SCEC) Community Velocity Model (CVM), a 3-D seismic velocity model for southern California (Magistrale et al. 2000).

For the current investigation, we compute long-period ground motion in the SCEC CVM for a suite of 60 earthquake scenarios. The 3-component ground motion time histories from these scenarios are saved on a grid of 1600 sites covering the Los Angeles region, including sites in the Los Angeles, San Fernando, and San Gabriel basins, as well as rock sites in the intervening areas. The results from the study take 2 forms: (1) We have saved and archived a library of time histories from the 60 scenarios. In cooperation with the SCEC Community Modeling Environment project, these time histories are available online, through a web interface specialized to engineering applications (<http://sceclib.sdsc.edu/LAWeb>). These long-period time histories capture basin amplifications, rupture-propagation-induced directivity, and 3-D seismic focusing phenomena. They are suitable for the engineering analyses of large, long-period structures, and smaller structures undergoing large, nonlinear deformations. (2) The results of the simulation suite have been analyzed to estimate response spectral amplification effects as a function of basin depth and period. The resulting mean response has been characterized parametrically and provided to the Next Generation Attenuation (NGA) project (Power et al. 2008) to guide development of attenuation relations in the empirical (NGA-E) phase of the project.

## COMPUTATIONAL METHODS

The computational program was a multi-institutional collaboration requiring major computing resources. In order to make effective use of supercomputing resources available to the respective collaborators, as well as to have cross-checks on the methodology, we employed five independently developed 3D wave propagation codes to do the numerical simulations. Four of these are FD codes (Olsen 1994; Larsen and Schultz 1995; Graves 1996; Pitarka 1999). These four are very similar in their mathematical formulation. Each uses a uniform, structured, cubic mesh, with staggered locations of the velocity and stress components, and a differencing scheme that is fourth-order accurate in space and second-order accurate in time. The codes differ in their computational approaches, their implementation of absorbing boundary conditions, and their implementation of anelastic attenuation. We used a FE code (Bao et al. 1998) for some of the simulations. The FE code uses unstructured meshing, and is second-order accurate in space and time.

Two of the FD schemes (Olsen, Graves) approximate a frequency-independent seismic quality factor ( $Q$ ) by implementing anelastic losses using the coarse memory variables representation (Day 1998; Day and Bradley 2001; Graves and Day 2003). Another (Larsen) uses a standard linear solid formulation that represents the absorption spectrum with a single Debye peak. The fourth FD scheme (Pitarka) represents attenuation by the method of Graves (1996), which is equivalent to mass-proportional Rayleigh damping and results in  $Q$  proportional to frequency (i.e., a red absorption spectrum). The FE scheme also uses the mass-proportional Rayleigh damping approximation to represent anelastic loss.

Comparison of results among these codes is useful for verifying the mathematical soundness of the five simulation codes. Such comparisons also permit assessment of any artifacts attributable to the absorbing boundary and attenuation implementations. Day et al. (2001, 2003) carried out a set of test simulations using all five codes. The comparisons between FD and FE solutions are particularly informative, as they permit an assessment of solution variability introduced by the model discretization. We show an example of such a comparison in a later section. The comparisons verify that all five codes are accurate for the class of problems relevant to this study.

These tests also enabled us to improve computational efficiency by modifying the SCEC CVM to eliminate very low seismic wavespeeds. Computing time is sensitive to the ratio of highest to lowest wavespeed present in the model, with low-wavespeed volumes requiring finer meshing than high-wavespeed volumes to ensure a given accuracy over a given bandwidth. The unstructured meshing possible with the FE method permitted us to perform a few simulations that include the very low-velocity, near-surface sediments present in the CVM ( $S$  velocity as low as 180 m/s). We compared these with calculations in which we put a lower threshold on the velocity model to exclude  $S$  wave velocity values in the CVM that fall below 500 m/s (replacing the lower values with the 500 m/s threshold value). The tests confirm that imposing this threshold (for the sake of computational efficiency) has negligible effect within the target bandwidth of 0–0.5 Hz.

Olsen et al. (2003) carried out simulations of the 1994 Northridge, California, earthquake, using the SCEC CVM, with the same FD method used in the current study, and their comparisons of synthetic and recorded ground velocities demonstrate the ability of the numerical modeling procedures to capture basin amplification effects. Further validation is provided by comparison of synthetic (FD and FE) and recorded seismic waveforms of small southern California earthquakes. For example, Chen et al. (2007) find that FD synthetics computed with the SCEC CVM model give a variance reduction of greater than 60% in both phase-delay times and log of amplitude, relative to a standard 1-D model. Additional validation for the velocity structure used in this study is provided by sonic log data, on the basis of which Stewart et al. (2005) estimate that uncertainties in basin depth in the SCEC CVM introduce uncertainties in ground motion (up to 0.1 natural log units) that they judge to be small compared with typical error terms in attenuation relations.

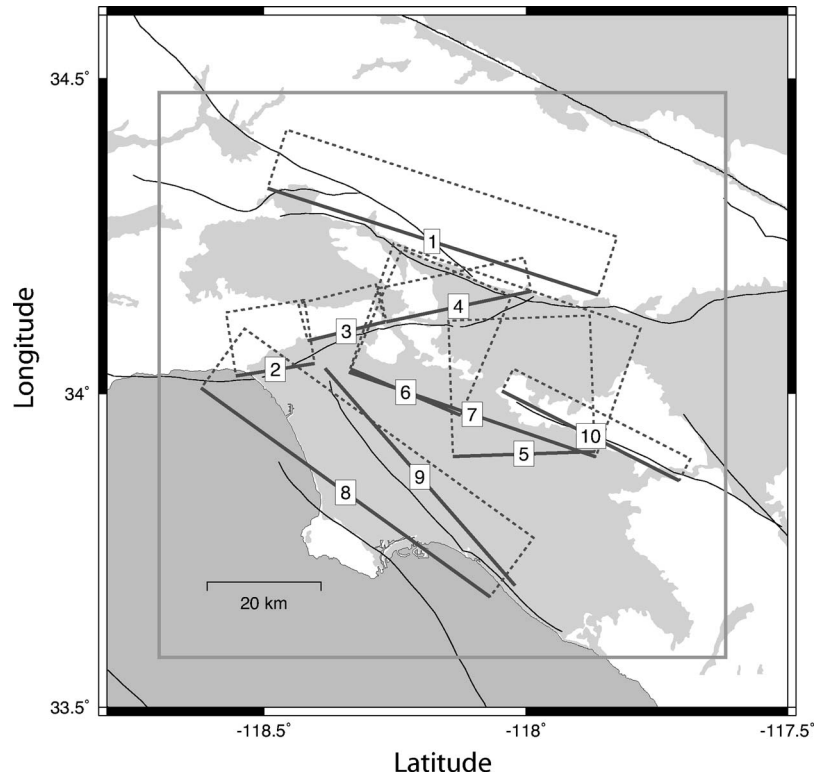


**Figure 1.** Map of scenario events and model region. See Table 1 for fault names and event magnitudes. Each rectangle is the surface projection of one of the faults, with the upper edge shown as a solid line and the other three edges shown as dashed lines. The large gray rectangle indicates the computational domain of the simulations.

### EARTHQUAKE SCENARIOS

We model sources on ten different faults, or fault configurations (for example, the Puente Hills fault is modeled in 3 different segmentation configurations). For each fault, we simulate 6 sources, using combinations of 3 different static slip distributions and 2 hypocenter locations. These are kinematic simulations: Rupture velocity, static slip, and the form of the slip velocity function are all specified *a priori*.

The areal coverage for the 3-D models is the  $100\text{ km} \times 100\text{ km}$  region outlined by the large gray box in Figure 1. In all simulations, the boundaries of the computational domain (i.e., absorbing boundaries) lie at or outside of this area and extend to a depth of at least 30 km. For the FD calculations, a uniform grid spacing of 200 m was used. The FE grid uses a variable element size, with near-surface elements as small as 30 m in dimension.

**Table 1.** List of fault rupture scenarios

| Fault    | Lon      | Lat    | $M_w$ | Length | Width | Strike | Dip | Rake | Depth | $\tau_r$ |
|----------|----------|--------|-------|--------|-------|--------|-----|------|-------|----------|
| 1)smad   | -118.178 | 34.242 | 7.0   | 61     | 18    | 288    | 53  | 90   | 0     | 1.4      |
| 2)smon1  | -118.479 | 34.039 | 6.3   | 14     | 14    | 261    | 36  | 45   | 1     | 0.63     |
| 3)hwood  | -118.343 | 34.099 | 6.4   | 14     | 19    | 256    | 69  | 70   | 0     | 0.71     |
| 4)raym2  | -118.128 | 34.139 | 6.6   | 26     | 17    | 258    | 69  | 70   | 0     | 0.89     |
| 5)ph2e   | -118.004 | 33.904 | 6.8   | 25     | 27    | 268    | 27  | 90   | 3     | 1.1      |
| 6)phla   | -118.228 | 34.003 | 6.7   | 21     | 26    | 293    | 28  | 90   | 3     | 1.0      |
| 7)phall  | -118.102 | 33.967 | 7.1   | 46     | 27    | 289    | 27  | 90   | 2     | 1.6      |
| 8)comp   | -118.344 | 33.843 | 6.9   | 63     | 14    | 306    | 22  | 90   | 5     | 1.3      |
| 9)nin    | -118.202 | 33.868 | 6.9   | 51     | 16    | 319    | 90  | 180  | 0     | 1.3      |
| 10)whitn | -117.876 | 33.933 | 6.7   | 35     | 15    | 297    | 73  | 180  | 0     | 1.0      |

(1) Lengths in kilometers, times in seconds, angles in degrees

(2)  $\tau_r$  is slip duration (from Equation 1)

(3) Geographical and depth coordinates refer to center of upper fault edge

(4) Faults are Sierra Madre (smad), Santa Monica (smon1), Hollywood (hwood), Puente Hills (northern segment is ph2e, southern segment is phla, combined scenario is phall), Compton (comp), Newport-Inglewood (nin), and Whittier (whitn).

We use the 10 faults listed in Table 1 for the scenario calculations. The fault surfaces are simplified representations of the fault geometry given by the SCEC Community Fault Model, and our choice of rupture scenarios was guided in part by the geologic considerations surveyed by Dolan et al. (1995). The surface projections of these faults are also shown in Figure 1. The longitude and latitude coordinates in this table refer to the geographic location of the top center of the fault, that is, the point on the surface that is directly above the midpoint of the top edge of the fault. Strike, dip and rake follow Aki and Richards' (1980) convention. Length, width and depth are all given in km. The depth refers to the depth below the surface of the top edge of the fault (0 corresponding to a surface-rupturing event).

For each of the fault geometries, we generate 3 random slip distributions, as realizations of a stochastic model, for use in the simulations. The slip distributions are generated following some empirical rules for the size and distribution of asperities as given by Somerville et al. (1999). The slip values on the fault are drawn from a uniformly distributed random variable, then spatially filtered to give a spectral decay inversely proportional to wavenumber squared, with a corner wavenumber at approximately  $1/L$ , where  $L$  is fault length. Finally, the slip values are scaled to the target moment of the scenario. As an example, Figure 2 shows the slip distribution functions generated by this procedure for one of the faults (Compton, fault number 8 in Figure 1). The two hypocenter locations (shown as stars in Figure 2) are defined as follows for each fault: Hypocenter 1 is located at an along-strike distance of 0.25 of the fault length and at a down-dip distance of 0.7 of the fault width (measured within the fault plane from the top edge of the fault, not the ground surface). Hypocenter 2 is located at an along strike distance of 0.75 of the fault length and at a down-dip distance of 0.7 of the fault width.

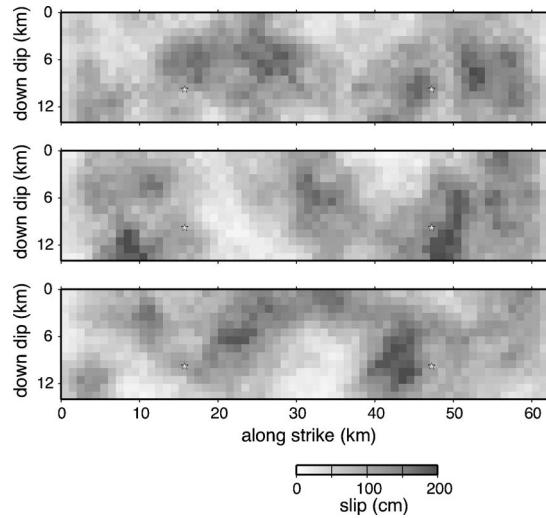


**Figure 2.** The three slip distributions and two hypocenter locations (stars) used in combination to provide sources for the six Compton Fault simulations. The distributions were generated by the stochastic approach described in the text.

The slip velocity function for each simulation is an isosceles triangle with a base of duration  $\tau_r$ . The value of  $\tau_r$  is magnitude dependent and given by the empirically derived expression (Somerville et al. 1999):

$$\log_{10} \tau_r = 0.5M_w - 3.35, \quad (1)$$

where  $M_w$  is moment magnitude and  $\tau_r$  is in seconds. Values used for  $\tau_r$  are given in Table 1. Rupture velocity is constant for all faults and all slip models. This value is set at 2.8 km/s. The rupture starts at the hypocenter and spreads radially outward from this point at the specified velocity. The simulated duration for each scenario is 80 seconds.

All simulations use the SCEC CVM, Version 2, except for modifications described below to impose a lower limit on the velocities and add anelastic attenuation. The unmodified model is described in Magistrale et al. (2000). The SCEC model is modified as follows: We replace the SCEC model  $S$  velocity with the value 500 m/s whenever the SCEC model value falls below 500 m/s. Whenever this minimum  $S$  velocity is imposed, the  $P$  wave velocity is set equal to 3 times the  $S$  velocity (1500 m/s in this case). Density values follow the SCEC model without modification. The quality factors for  $P$  and  $S$  waves, respectively,  $Q_p$  and  $Q_s$ , are set to the preferred  $Q$  model of Olsen et al. (2003).

The 3-component time histories are saved on a 2 km  $\times$  2 km grid covering the inner 80 km  $\times$  80 km portion of the model area (Figure 3). No filtering is applied to the output. The resulting synthetic data set contains 3-component records for 1600 sites (4800 time histories) for each scenario simulation. For all 60 scenarios, and all sites, we compute response spectral acceleration (Sa), for 5% damping, as a function of period, for

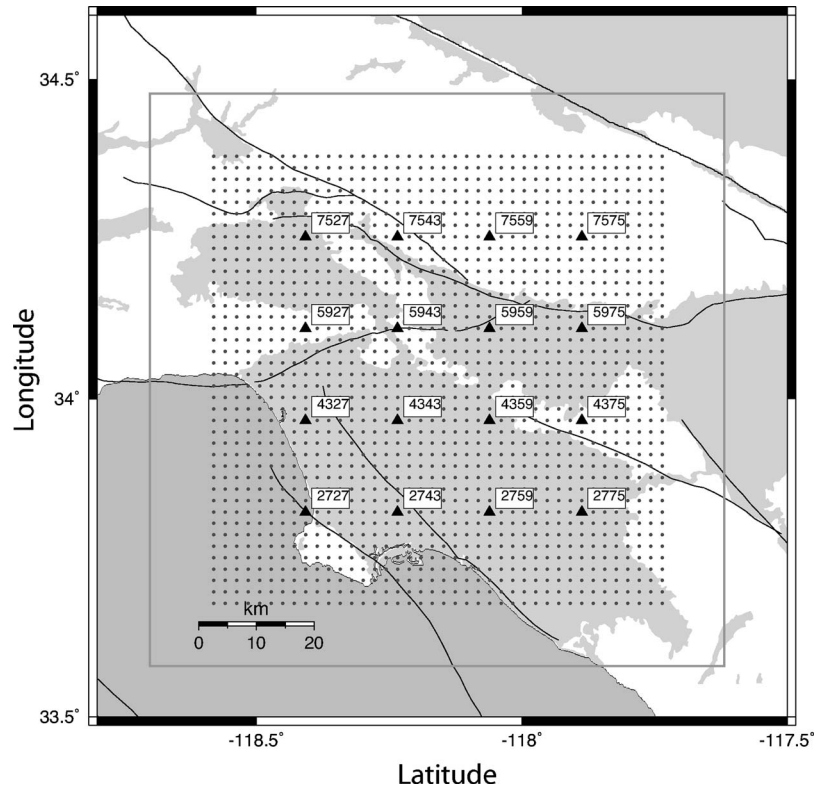


**Figure 3.** Map showing the grid of time-history output sites (dots). Sites shown as triangles are those at which we cross-checked results from difference simulation codes.

each component of motion. This is done for 26 periods in the range 2–10 seconds: Spectral acceleration is computed at 0.2 second intervals between 2 and 5 seconds, and at 0.5 second intervals between 5 and 10 seconds.

The earthquake scenarios in this study are limited to events on faults near or within the main sedimentary basins of the Los Angeles region. We have excluded earthquake scenarios for the more distant San Andreas fault, for which several earthquake scenarios of  $M_w$  greater than 7.5 have been proposed (e.g., Working Group on California Earthquake Probabilities 1995). Olsen et al. (2006; 2008) simulate large San Andreas fault earthquakes, finding unusually strong basin effects for some events. In particular, in their simulations the sequence of basins south of the Transverse Ranges, between the San Andreas and Los Angeles, acts as a waveguide. The resultant channeling of seismic energy into the Los Angeles region produces anomalously high amplitudes at some relatively distant basin sites.

## COMPARISON OF FE AND FD SOLUTIONS

As noted above, the FD simulations used a uniform grid spacing of 200 m. Since seismic velocities as low as 500 m/s are present in the model, and the target frequency band of the simulations is 0–0.5 Hz, the FD simulations resolve the minimum wavelength with about 5 grid intervals. At this resolution, phase-velocity errors over homogeneous paths are typically very small (for the fourth-order staggered-grid FD method used here), of the order of 1% or less (Levander 1988). However, it is difficult to translate this measure of accuracy into accuracy of ground motion time histories calculated over complex paths. To confirm that the FD simulations indeed predict ground motion time histories accurately within our target frequency band, we repeated some of them using the FE method, with a highly oversampled mesh (feasible because of the unstructured meshing capability of the FE method). The FE simulations employed node spacing as small as 30 m in the low-velocity parts of the model. Thus, even accounting for the approximate factor of two difference in points-per-wavelength requirement for a given phase-velocity accuracy between the (fourth-order accurate) FD method and the (second-order accurate) FE method, the FE simulations can be expected to have about three times better resolution of the minimum wavelength in the basins. Figure 4 compares three-component velocity time-histories for one of the scenarios (Newport-Inglewood fault), as computed by FE and FD methods, respectively. The time histories are for the 16 locations denoted by triangles in Figure 3. In nearly all cases the differences between the solutions are negligible, in that relative phase-delay times for the dominant arrivals never exceed a few tenths of a second, and their amplitude differences rarely reach 10%.

Figure 5 provides a quantitative comparison in the frequency domain. The figure was constructed from smoothed (0.1 Hz band averages) Fourier spectra of the 16 FD and 16 FE EW-component velocity time histories in Figure 4. The figure shows means and standard deviations (over the 16 recordings) of the natural logarithm of the FD to FE spectral ratio, for each independent frequency band. The FD/FE bias is less than 10% (and scatter less than 25%) for all frequencies in our target band of 0–0.5 Hz. Given the heavy oversampling achieved for the FE solution, this agreement provides strong evidence that both methods have adequate resolution to be accurate throughout the target frequency band. It also shows that there are no significant biases introduced by the different ways in which the two methods model anelastic attenuation.

We have made similar comparisons for 10 such simulation pairs (i.e., comparing results from either a pair of FD codes or from an FD FE pair). Because the FD and FE computational meshes are very different, sampling the SCEC CVM at different points (and with much higher resolution in the near surface in the case of the FE grid), the FE/FD comparison represents the worst case for achieving agreement between codes. Simulations of the same scenario computed with different FD codes produce time histories and spectra that are almost indistinguishable.

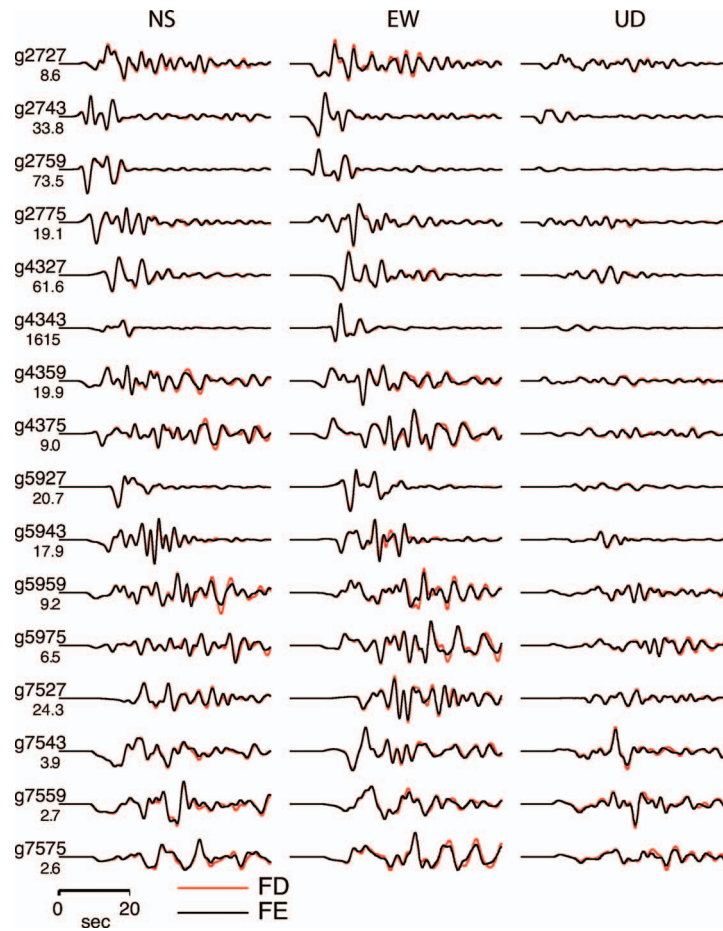


**Figure 4.** Comparison of finite element and finite difference solutions for one of the Newport-Inglewood rupture-scenario simulations. Velocity time histories are shown for the 16 sites shown as triangles in Figure 3. North-south (NS), east-west (EW) and up-down (UD) component traces are given. The upper number of each pair on the left designates the station number, as given in Figure 3. The lower number of each pair gives the peak velocity (for the component having the largest peak), in cm/s.

### REFERENCE SIMULATIONS

To aid us in quantifying the effect of sedimentary basins on the computed ground motions, we perform several auxiliary, or “reference,” simulations (using the same FE and FD methods used for all the other simulations). For each of the 10 faults, we select one rupture scenario, and repeat that simulation using the same source model, but replacing the SCEC CVM with a horizontally stratified (1-D) model. The stratified reference model corresponds to an artificially high-velocity, unweathered hard-rock site. This reference velocity model was constructed by laterally extending a vertical profile of the

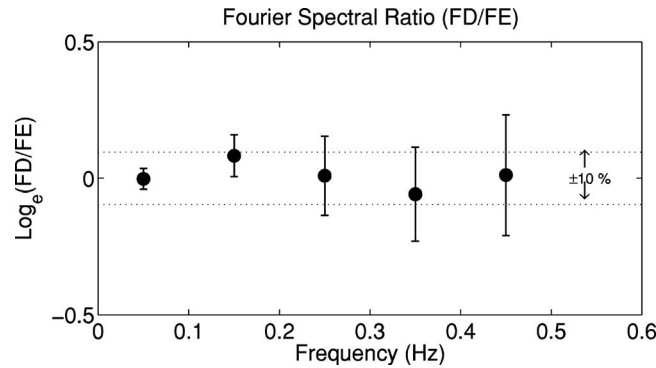


**Figure 5.** Ratio of smoothed (over 0.1 Hz bands) Fourier spectra of the EW-component FD and FE solutions shown in Figure 4. Solid circles are averages (over the 16 sites) of the natural logarithm of the FD to FE spectral ratio, and error bars give the corresponding standard deviations.

SCEC CVM located at  $(-118.08333, 34.29167)$ , in the San Gabriel Mountains. As noted, surface  $S$  velocities are artificially high (3.2 km/s) in the resulting model, since this part of the SCEC model does not account for a weathered layer. The principal purpose of the reference simulations is to provide a spectral normalization for the results from the simulations done in the full SCEC CMV, as an approximate means of isolating basin effects from source effects.

Figure 6 shows velocity time histories for a Newport-Inglewood scenario (source and recording sites are the same as used for the FD/FE comparison shown in Figure 4). The figure compares three-component velocities for the simulation done with the SCEC CVM with the corresponding velocities for the reference simulation. The comparison gives an idea of the importance of 3-D structure, which introduces effects that are especially pronounced at long period and late in the time series.

## RESPONSE SPECTRAL AMPLIFICATIONS

Basin amplification effects result from interaction of the wavefield with basin margins, and depend in a complex, poorly understood manner on period, source location, source distance, basin geometry, sediment velocity distribution, and site location within the basin. The 60 scenarios provide synthetic data that can be used to improve our understanding of these effects. We take an initial step in this direction by attempting to isolate the effects of period and local basin depth. To isolate these two effects, we average over sources. As response spectral values vary much more between ruptures on different faults than between ruptures on a given fault, we have computed averages using only 1 of the 6 scenarios from each fault, giving us a 10-event subset of the simulations. This subset misses a small amount of the variability in basin response present in the full 60-event suite, but allows us to work with spectral values normalized to the reference

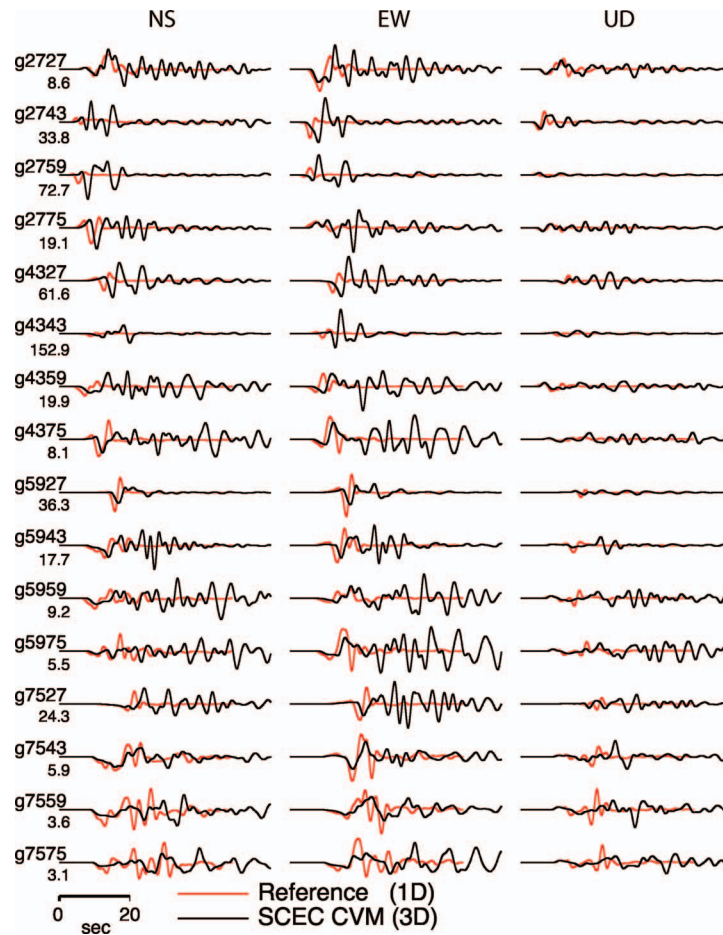


**Figure 6.** Comparison of time histories for one of the 3D (SCEC CVM) simulations (Newport-Inglewood rupture scenario) with the time histories for the corresponding reference (1-D rock model) simulation.

structure, without requiring 60 reference-structure simulations. Tests using a small number of additional events confirm that source effects have been adequately removed by this procedure.

The synthetic time histories are band limited, and, although there is no abrupt spectral cutoff at the 0.5 Hz limit, the synthetics rapidly become spectrally deficient above this frequency. This limitation will have the effect of biasing response spectral estimates downward at frequencies near, yet still below, the 0.5 Hz cutoff (since each response spectral ordinate is a finite-bandwidth measure of ground motion), compared with values that would be calculated from full-bandwidth time histories. We have made a quantitative estimate of this bias by calculating response spectra from 25 recordings of the 1992

Landers, California, earthquake. We calculated the response spectra both before and after applying a low-pass filter to remove Fourier spectral components above 0.5 Hz. At a period of 2 s (i.e., right at the upper frequency cutoff), the low-passed case has its response spectrum biased downward by 45%. However, at 3 s period the bias is only 15% and falls rapidly as the period lengthens further (e.g., to 4% at 4 s). The actual bias in our case will be even lower, as the synthetics do not have as sharp a spectral cutoff as we created by filtering the Landers earthquake data. Furthermore, any bias will be further reduced because our presentation is in terms of spectral ratios. That is, in all cases we normalize the response spectra by dividing them by response spectra for reference solutions that have the same Fourier spectral limits (and as a result have similar response-spectral bias). The effectiveness of the normalization in removing the short-period bias is difficult to quantify, but is qualitatively supported by the consistency and smoothness with which the 2 s spectra extrapolate trends defined at longer period (as seen in the results to be presented later). Therefore, we present the normalized response spectra for periods as low as 2 s, but the ordinates at periods below 3 s should be interpreted with caution; only at periods of 3 s and longer do we have quantitative corroboration that the response spectra are nearly unbiased (i.e., within  $\sim 15\%$  tolerance).

## METHOD

We first bin the sites according to the local basin depth  $D$  at a site, with  $D_j$  denoting the depth at site  $j$ . For this purpose, we define the depth  $D$  to be the depth to a specified  $S$ -wave velocity isosurface. We present results for the case  $D=Z_{1.5}$ , where  $Z_{1.5}$  is depth to the 1.5 km/s isosurface. Note, however, that in the SCEC CVM, the depths of different  $S$  velocity isosurfaces are strongly correlated, and therefore very similar results (apart from a scaling of the depth variable) are obtained using the 1.0 or 2.5 km/s isosurface ( $Z_{1.0}$  or  $Z_{2.5}$ ) instead of the 1.5 km/s isosurface. The binning is represented through a matrix  $W$ . We define  $N_{\text{bin}}$  bins by specifying depths  $D_q^{\text{bin}}$ ,  $q=1, \dots, N_{\text{bin}}$ , at the bin centers, spaced at equal intervals  $\Delta D$  (i.e.,  $D_q^{\text{bin}}=(q-1/2)\Delta D$ ), and then form  $W$ ,

$$W_{qj} = \begin{cases} 1 & \text{if } (D_q^{\text{bin}} - \Delta D/2) \leq D_j < (D_q^{\text{bin}} + \Delta D/2) \\ 0 & \text{otherwise} \end{cases}. \quad (2)$$

For consistency with most empirical attenuation relations, we work with response spectral values averaged over the two horizontal components. For the  $i$ th event and  $j$ th site, we form the ratio  $Sa_{ij}(T_k)/Sa_{ij}^{\text{ref}}(T_k)$ , where  $Sa_{ij}(T_k)$  is the absolute spectral acceleration (geometrical mean of the two horizontal components) from SCEC-CVM event  $i$  at site  $j$  and period  $T_k$ , and  $Sa_{ij}^{\text{ref}}(T_k)$  is the corresponding quantity for the corresponding reference-model event. Then we form the source-averaged basin response factor  $B(D_q, T_k)$  by taking the natural logarithm and averaging over all  $N_{\text{site}}$  sites ( $N_{\text{site}}=1600$ ), and over all  $N_{\text{ev}}$  events, where in this case  $N_{\text{ev}}$  is 10:

$$B(D_q, T_k) = \left( N_{\text{ev}} \sum_{j=1}^{N_{\text{site}}} W_{qj} \right)^{-1} \sum_{i=1}^{N_{\text{ev}}} \sum_{j=1}^{N_{\text{site}}} W_{qj} \ln[Sa_{ij}(T_k)/Sa_{ij}^{\text{ref}}(T_k)]. \quad (3)$$

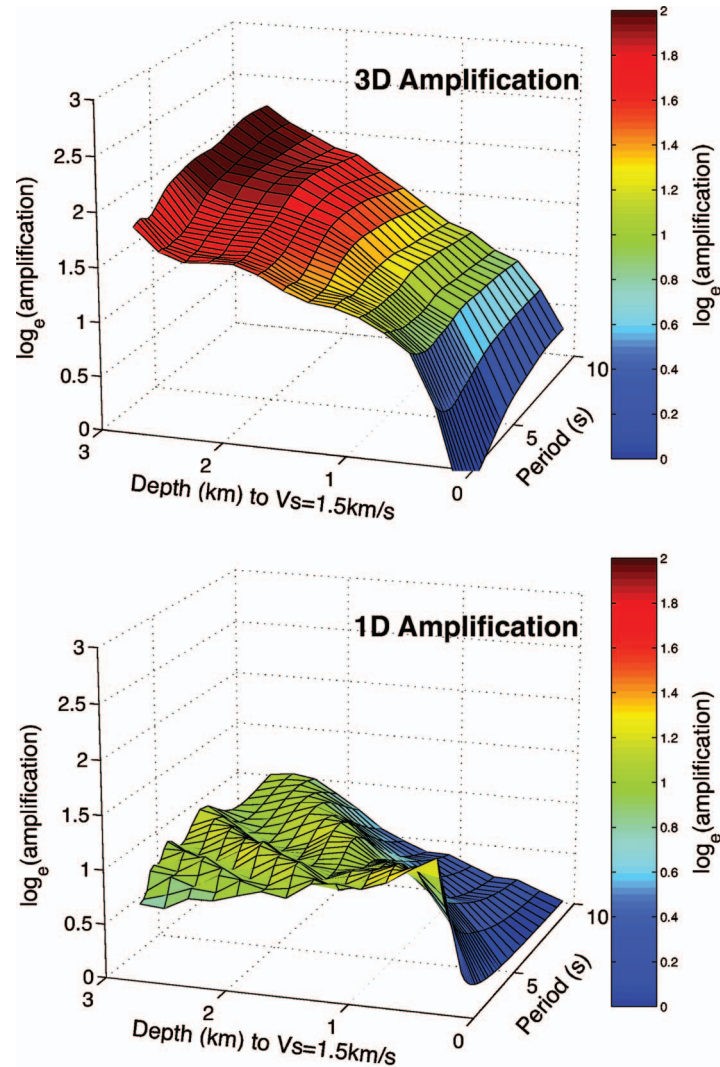


**Figure 7.** Top: Natural logarithm of basin amplification versus depth (to 1.5 km/s  $S$ -velocity isosurface) and period, calculated from 3D simulations. Bottom: Natural logarithm of basin amplification calculated by same procedure, but replacing the 3D results with 1-D plane-wave amplification factors calculated using the local 1-D wavespeed and density profiles (from the SCEC CVM) at each of the 1600 sites.

## RESULTS

Figure 7 summarizes the results of this procedure (for 200 m bins). The upper frame shows  $B$  as a function of depth and period. The lower frame shows basin amplification calculated by the same procedure, but replacing the spectral acceleration ratio  $Sa_{ij}(T_k)/Sa_{ij}^{ref}(T_k)$  at each site by the vertically incident plane-wave amplification factor

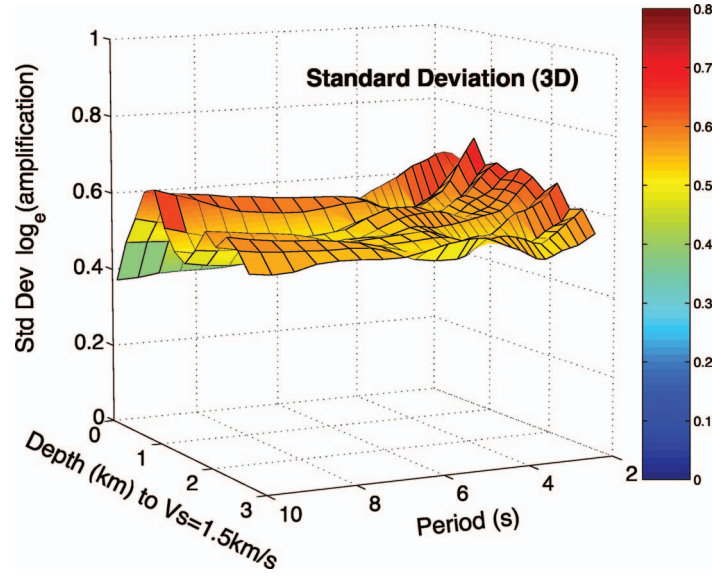


**Figure 8.** Standard deviation of the natural logarithm of basin amplification, as function of depth and period, from the 3D simulations.

for that site. The latter factors were computed using a plane-layered structure specific to each site, and corresponding to the SCEC-CVM shear wavespeed and density depth-profiles directly beneath that site. The main results from Figure 7 are the following: (1) Source-averaged basin amplification is period dependent, with the highest amplifications occurring for the longest periods and greatest basin depths. (2) Relative to the very-hard rock reference structure, the maximum amplification is about a factor of 8. (3) Compared with 1-D theoretical predictions, the 3-D response is in most cases substantially higher. (4) The 3-D response is also smoother, as a function of depth and period, than is the 1-D prediction. We attribute the smoother depth and period dependence to the presence of laterally propagating waves in the 3-D case that smooth out the resonances present in the 1-D case.

Figure 8 shows the standard deviations  $s$  of the logarithm of amplification, as a function of depth and period, that is,

$$s^2(D_q, T_k) = \left( N_{ev} \sum_{j=1}^{N_{site}} W_{qj} \right)^{-1} \sum_{i=1}^{N_{ev}} \sum_{j=1}^{N_{site}} W_{qj} \{ \ln[Sa_{ij}(T_k)/Sa_{ij}^{ref}(T_k)] - B(D_q, T_k) \}^2. \quad (4)$$

Most values fall between 0.5 and 0.6, and there is a mild tendency for  $s$  to increase at the short-period end of our range. The differences are small, but some period-dependence of this sort is what one might expect on the basis of simple physical arguments. Short-period waves are subject to short-wavelength variations due to local focus-

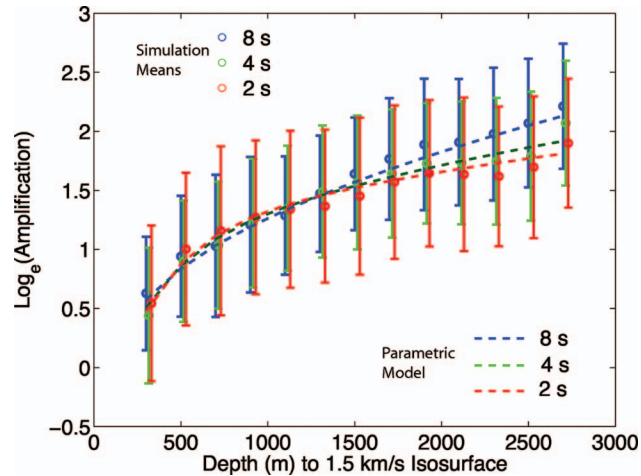


**Figure 9.** Natural logarithm of the basin amplification factor, as a function of depth to the 1.5 km/s  $S$  velocity isosurface. Solid circles of a given color represent the mean amplification factor for one response-spectral period, and the error bars give the standard deviations. For clarity, only three periods (2, 4, and 8 s) are shown, out of the 26 periods calculated. Further numerical results are given in Table 2. The dashed curves are the corresponding basin amplification factors calculated from the parametric model (Equation 5a and 5b and Table 3) fit to the 3D simulation results.

ing and interference effects. Very long-period waves, in contrast, represent oscillations that are coherent over large scale lengths and are influenced principally by large-scale averages of the seismic velocity structure.

Figure 9 presents the basin-depth dependence of  $B$  in the form of mean amplification values (open circles) and their standard deviations (vertical bars) for each of 3 periods (2, 4, and 8 s). For depths ( $Z_{1.5}$ ) in the range of roughly 500–1000 m, mean amplification tends to decrease slightly with period, though the effect is small compared with the scatter. This result is, at least qualitatively, in agreement with expectations from 1-D theory: Shallow sediments will have diminished effect as the wavelength becomes long relative to sediment depth. For depths exceeding about 2000 m, mean amplification increases systematically with period. This is a 3-D effect: Higher-mode resonances present in the 1-D case are smoothed out by lateral scattering, so that the longer-period resonances dominate. Numerical values of  $B$  are given in Table 2 for a range of representative periods and depths.

### PARAMETRIC MODEL

It is useful to have a simple functional form that captures the main elements of the period- and depth-dependent basin amplification behavior observed in the simulations. One purpose of such a representation is to provide a functional form for representing basin effects in regression modeling of empirical ground motion data. We constructed a

**Table 2.** Mean (and standard deviation) of natural log of amplification, versus basin depth and period

| $Z_{1.5}$<br>(km) | Period (s) |            |            |            |            |            |            |
|-------------------|------------|------------|------------|------------|------------|------------|------------|
|                   | 2          | 3          | 4          | 5          | 6          | 8          | 10         |
| 0.3               | 0.54(0.66) | 0.38(0.63) | 0.44(0.57) | 0.52(0.55) | 0.59(0.54) | 0.63(0.48) | 0.63(0.48) |
| 0.5               | 1.00(0.65) | 0.89(0.55) | 0.90(0.51) | 0.94(0.53) | 0.97(0.54) | 0.94(0.51) | 0.89(0.55) |
| 0.7               | 1.16(0.72) | 1.07(0.57) | 1.04(0.54) | 1.05(0.58) | 1.08(0.59) | 1.03(0.60) | 0.98(0.63) |
| 0.9               | 1.27(0.65) | 1.23(0.54) | 1.22(0.54) | 1.25(0.58) | 1.28(0.57) | 1.21(0.57) | 1.13(0.64) |
| 1.1               | 1.34(0.66) | 1.32(0.58) | 1.35(0.53) | 1.37(0.53) | 1.36(0.51) | 1.29(0.50) | 1.21(0.56) |
| 1.3               | 1.37(0.65) | 1.37(0.57) | 1.49(0.56) | 1.56(0.57) | 1.55(0.53) | 1.47(0.49) | 1.36(0.51) |
| 1.5               | 1.45(0.66) | 1.44(0.56) | 1.57(0.57) | 1.69(0.56) | 1.71(0.51) | 1.64(0.48) | 1.51(0.48) |
| 1.7               | 1.57(0.65) | 1.57(0.56) | 1.64(0.54) | 1.76(0.54) | 1.81(0.53) | 1.77(0.52) | 1.65(0.53) |
| 1.9               | 1.64(0.62) | 1.64(0.53) | 1.73(0.51) | 1.83(0.54) | 1.92(0.53) | 1.89(0.56) | 1.80(0.58) |
| 2.1               | 1.64(0.65) | 1.63(0.58) | 1.73(0.52) | 1.84(0.53) | 1.92(0.53) | 1.91(0.53) | 1.85(0.55) |
| 2.3               | 1.62(0.59) | 1.65(0.51) | 1.75(0.54) | 1.87(0.51) | 1.97(0.52) | 1.98(0.56) | 1.96(0.59) |
| 2.5               | 1.70(0.60) | 1.70(0.52) | 1.79(0.55) | 1.94(0.50) | 1.99(0.51) | 2.07(0.55) | 2.06(0.56) |
| 2.7               | 1.90(0.55) | 1.90(0.50) | 2.07(0.53) | 2.13(0.56) | 2.15(0.54) | 2.21(0.53) | 2.21(0.51) |

preliminary representation of this sort to provide guidance to the NGA development teams. Our approximate representation,  $\tilde{B}(D, T)$  takes the following form:

$$\tilde{B}(D, T) = a_0(T) + a_1(T)[1 - \exp(D/300)] + a_2(T)[1 - \exp(D/4000)], \quad (5a)$$

where

$$a_i(T) = b_i + c_i T, \quad i = 0, 1, 2, \quad (5b)$$

with  $T$  given in seconds and  $D$  in meters. This functional form is not itself based directly upon physical considerations, but rather serves to summarize the practical results of the simulations (which of course are themselves based on the physics of seismic wave propagation). The particular function in Equation 5a and 5b was chosen because (i) it allows for a basin-depth dependence with decreasing slope at increasing values of the depth parameter, as required to capture the behavior shown in Figure 9, and (ii) it permits the depth dependence to vary with period, as also required by Figure 9. The 6 parameters  $b_i$ ,  $c_i$  were calculated in a two-step procedure. Separate least squares fits (at each period  $T_k$ ) of  $\tilde{B}(D, T_k)$  to  $B(D_q, T_k)$  gave individual estimates of the  $a_i(T_k)$  values for each period  $T_k$ . Then parameters  $b_i$  and  $c_i$ , for each  $i=0, 1, 2$ , were obtained by least-squares fitting of these 26 individual  $a_i(T_k)$  estimates. The resulting values are shown in Table 3. We repeated the full analysis (normalizing, binning, and parameter fitting) using the 1.0 and 2.5 km/s isosurfaces, respectively, as depth parameters (i.e., setting  $D=Z_{1.0}$  and  $D=Z_{2.5}$ , respectively), and those results are also shown in Table 3.

**Table 3.** Coefficients for basin amplification factor (Equations 5a and 5b)

| Isosurface<br>Depth (km) | $b_0$  | $b_1$ | $b_2$ | $c_0$ | $c_1$  | $c_2$ |
|--------------------------|--------|-------|-------|-------|--------|-------|
| 1.0                      | -0.609 | 2.26  | 0.421 | 0.083 | -0.189 | 0.560 |
| 1.5                      | -1.06  | 2.26  | 1.04  | 0.124 | -0.198 | 0.261 |
| 2.5                      | -0.95  | 1.35  | 1.84  | 0.132 | -0.167 | 0.091 |

Three of the resulting amplification curves (obtained by evaluating Equations 5a and 5b), for periods 2, 4, and 8 s, are shown as dashed curves in Figure 9. These expressions, despite their simplicity, represent the mean predictions of the numerical simulations quite well, and can serve as a starting point for modeling basin effects in empirical studies. Because they give a compact representation of complex wave propagation effects captured by the numerical simulations, they provide a physical basis for extrapolation of empirical models to periods greater than 2 or 3 seconds, where reliable data on basin effects are especially scarce. The standard deviations  $s$  of the simulation results, given in Figure 9 and Table 2, provide appropriate estimates of the standard errors of prediction for use with Equations 5a and 5b (the misfit of Equations 5a and 5b to  $B$  is very small compared with  $s$ , and has negligible effect on the prediction error).

## DISCUSSION AND CONCLUSIONS

We have characterized the source-averaged effect of basin depth on spectral acceleration using depth to the 1.5 km/s  $S$  velocity isosurface ( $Z_{1.5}$ ) as the predictor variable. The resulting mean basin-depth effect is period dependent, and both smoother (as a function of period and depth) and higher in amplitude than predictions from local 1-D models. For example, relative to a reference hard-rock site, sites with  $Z_{1.5}$  equal to 2.5 km (corresponding to some of the deeper L.A. basin locations) have a predicted mean amplification factor of approximately 5.5 at 3 s period, and approximately 7.8 at 10 s period.

The basin amplification estimates described here are intended to guide the design of functional forms for use in attenuation relationships for elastic response spectra. In particular, they should be useful guides for extrapolating the period-dependence of basin terms to periods longer than a few seconds, where empirical data provide little constraint. More direct, quantitative use of the results may become possible in the future, however. The main requirement is that we first carefully assess the extent to which the basin effect, as defined and quantified in this study, is already accounted for implicitly in existing attenuation relationships, through (1) departures of the average “rock” site from our idealized reference model, and (2) correlation of basin depth with other predictor variables (such as  $V_{s30}$ , i.e., the average  $S$  velocity in the upper 30 m). A preliminary assessment of the reference model bias is presented in Day et al. (2005). They find that the reference-model simulations under-predict the rock regression model of Abrahamson and Silva (1997) by a factor of 2 at long period (5 seconds, which is much too long a period to be affected by any response spectral biases associated with bandwidth limi-

tations of the simulations, as discussed earlier). They argue that at the long periods considered, both source details and  $V_{S30}$  will have minimal effects, and that this factor of 2 is likely representative of a seismic velocity shift (between the average engineering rock site and the reference model) extending to depths of the order of half a kilometer or more.

The NGA relationships all use  $V_{S30}$  as a predictor variable. The correlation between  $V_{S30}$  and basin depth is sufficiently strong to complicate the identification of the basin effect in the residuals after having fit a regression model to  $V_{S30}$ . Chiou and Youngs (2006) tested the basin effect model proposed here (Equation 5) for three small (Mw 4-5) earthquakes in southern California, and found that the model compared very well with spectral amplifications observed at over two hundred broadband stations of the Southern California Seismic Network. However, they concluded that, because of the basin depth- $V_{S30}$  correlation, they would have had to remove the  $V_{S30}$  site term from their NGA relationship in order to use the basin term. Doing so would make sense from a physical standpoint, for the long periods (3–10 s) considered here, because simple wavelength arguments make it clear that  $V_{S30}$  is unlikely to have significant physical effect at long period, and it is predictive of long-period response only to the extent that it is statistically correlated with overall sediment thickness. However,  $V_{S30}$  information is widely available for strong motion recording sites, whereas  $Z_{1.5}$  (as well as  $Z_{1.0}$  and  $Z_{2.5}$ ) data are not available for all sites. Therefore, from a practical standpoint, Chiou and Youngs (2008) found it expedient to develop their NGA model with  $V_{S30}$  retained as a predictor variable even at long period, to which they added a  $Z_{1.0}$  term to capture that part of the basin effect not fully accounted for by the correlation between  $V_{S30}$  and  $Z_{1.0}$ . The correlation of basin effects with  $V_{S30}$  is discussed further by Choi et al. (2005), who propose data analysis procedures for separating these effects.

For their NGA model, Campbell and Bozorgnia (2008) were able to empirically identify a residual basin-depth effect after applying the  $V_{S30}$  term in their model, but only for sites for which  $Z_{2.5} < 3$  km (corresponding to  $Z_{1.5} < \sim 1.5$  km). For  $Z_{2.5} > 3$  km, they found existing data too sparse to extend the empirical model and its period dependence to greater sediment depth. Campbell and Bozorgnia's NGA model uses the parametric basin-effect model from the current study (Equations 5a and 5b) to extrapolate the basin term into the  $Z_{2.5} > 3$  km regime.

Our parametric model is based on simulations for the southern California region. That region is characterized by deep sedimentary basins with relatively low  $S$  wave velocity. Sedimentary basins in other regions can have significantly different characteristics. For example, the San Francisco Bay region of California is characterized by laterally juxtaposed geologic blocks having relatively high  $S$  velocity and relatively shallow basins (e.g., Santa Clara basin). There is thus a need for additional region-specific studies of basin amplification effects, including empirical analysis as well as further simulation-based analysis. In addition, simulations, including the ones done for this study, should be used to assess the utility of other predictor variables besides basin depth. As an example, Choi et al. (2005) have taken a step in this direction by examining the effect on spectral amplification of source location relative to basin boundaries.

## ACKNOWLEDGMENTS

We benefited from helpful reviews by Roberto Paolucci, Charles Langston, and an anonymous reviewer. This work was supported by Pacific Earthquake Engineering Research (PEER) Center Lifelines Program (Tasks 1A01, 1A02, and 1A03), the National Science Foundation under the Southern California Earthquake Center (SCEC) Community Modeling Environment Project (grant EAR-0122464), and by SCEC. SCEC is funded by NSF Cooperative Agreement EAR-0106924 and USGS Cooperative Agreement 02HQAG0008. The SCEC contribution number for this paper is 1101.

## REFERENCES

- Abrahamson, N. A., and Silva, W. J., 1997. Empirical response spectral attenuation relations for shallow crustal earthquakes, *Seismol. Res. Lett.* **68**, 94–127.
- Aki, K., and Richards, P. G., 1980. *Quantitative Seismology, Theory and Methods*, W. H. Freeman and Co., New York.
- Bao, H., Bielak, J., Ghattas, O., Kallivokas, L. F., O'Hallaron, D. R., Shewchuk, J. R., and Xu, J., 1998. Large-scale simulation of elastic wave propagation in heterogeneous media on parallel computers, *Comput. Methods Appl. Mech. Eng.* **152**, 85–102.
- Campbell, K. W., 1997. Empirical near-source attenuation relationships for horizontal and vertical components of peak ground acceleration, peak ground velocity, and pseudo-absolute acceleration response spectra, *Seismol. Res. Lett.* **68**, 154–179.
- Campbell, K. W., and Bozorgnia, Y., 2008. Campbell-Bozorgnia NGA horizontal ground motion model for PGA, PGV, PGD and 5% damped linear elastic response spectra, *Earthquake Spectra* **24**, 139–171.
- Chen, P., Zhao, L., and Jordan, T. H., 2007. Full 3-D tomography for crustal structure of the Los Angeles region, *Bull. Seismol. Soc. Am.* **97**, 1094–1120.
- Chiou, B. S.-J., and Youngs, R. R., 2006. Chiou and Youngs PEER-NGA empirical ground motion model for the average horizontal component of peak acceleration and pseudo-spectral acceleration for spectral periods of 0.01 to 10 seconds, PEER Report, [http://peer.berkeley.edu/products/Chiou\\_Youngs\\_NGA\\_2006.html](http://peer.berkeley.edu/products/Chiou_Youngs_NGA_2006.html).
- , 2008. An NGA model for the average horizontal component of peak ground motion and response spectra, *Earthquake Spectra* **24**, 173–215.
- Choi, Y., Stewart, J. P., and Graves, R. W., 2005. Empirical model for basin effects accounts for basin depth and source location, *Bull. Seismol. Soc. Am.* **95**, 1412–1427.
- Day, S. M., 1998. Efficient simulation of constant Q using coarse-grained memory variables, *Bull. Seismol. Soc. Am.* **88**, pp. 1051–1062.
- Day, S. M., and Bradley, C., 2001. Memory-efficient simulation of anelastic wave propagation, *Bull. Seismol. Soc. Am.* **91**, 520–531.
- Day, S. M., Bielak, J., Dreger, D., Graves, R. W., Larsen, S., Olsen, K. B., and Pitarka, A., 2001. *Tests of 3-D elastodynamic codes: Final report for Lifelines Project 1A01*, Pacific Earthquake Engineering Research Center.

- , 2003. *Tests of 3-D elastodynamic codes: Final report for Lifelines Project 1A02*, Pacific Earthquake Engineering Research Center.
- , 2005. *3-D ground motion simulation in basins: Final report for Lifelines Project 1A03*, Pacific Earthquake Engineering Research Center.
- Dolan, J. J., Sieh, K., Rockwell, T. K., Yeats, R. S., Shaw, J., Suppe, J., Huftile, G. J., and Gath, E. M., 1995. Prospects for larger or more frequent earthquakes in the Los Angeles Metropolitan region, *Science* **267**, 199–205.
- Field, E. H., 1996. Spectral amplification in a sediment-filled valley exhibiting clear basin-edge-induced waves, *Bull. Seismol. Soc. Am.* **86**, 991–1005.
- , 2000. A modified ground motion attenuation relationship for southern California that accounts for detailed site classification and a basin depth effect, *Bull. Seismol. Soc. Am.* **90**, S209–S221.
- Frankel, A., and Vidale, J., 1992. A three-dimensional simulation of seismic waves in the Santa Clara Valley, California, from a Loma Prieta aftershock, *Bull. Seismol. Soc. Am.* **82**, 2045–2074.
- Graves, R. W., 1996. Simulating seismic wave propagation in 3-D elastic media using staggered grid finite differences, *Bull. Seismol. Soc. Am.* Vol. **86**, 1091–1106.
- Graves, R. W., Pitarka, A., and Somerville, P. G., 1998. Ground-motion amplification in the Santa Monica area: Effects of shallow basin-edge structure, *Bull. Seismol. Soc. Am.* **88**, 1224–1242.
- Graves, R. W., and Day, S. M., 2003. Stability and accuracy of coarse-grain viscoelastic simulations, *Bull. Seismol. Soc. Am.* **93**, 283–300.
- Joyner, W. B., 2000. Strong motion from surface waves in deep sedimentary basins, *Bull. Seismol. Soc. Am.* **90**, S95–S112.
- King, J. L., and Tucker, B. E., 1984. Observed variations of earthquake motion across a sediment-filled valley, *Bull. Seismol. Soc. Am.* **74**, 137–151.
- Kohler, M., Magistrale, H., and Clayton, R., 2003. Mantle heterogeneities and the SCEC three-dimensional seismic velocity model version 3, *Bull. Seismol. Soc. Am.* **93**, 757–774.
- Komatitsch, D., Liu, Q., Tromp, J., Suss, P., Stidham, C., and Shaw, J. H., 2004. Simulations of ground motion in the Los Angeles basin based upon the spectral-element method, *Bull. Seismol. Soc. Am.* **94**, 187–206.
- Larsen, S., and Schultz, C. A., 1995. *ELAS3D: 2D/3D elastic finite-difference wave propagation code*, Technical Report No. UCRL-MA-121792, 19 pp.
- Levander, A. R., 1988. Fourth-order finite-difference P-SV seismograms, *Geophysics* **53**, 1425–1436.
- Magistrale, H., Day, S. M., Clayton, R., and Graves, R. W., 2000. The SCEC southern California reference three-dimensional seismic velocity model version 2, *Bull. Seismol. Soc. Am.* **90**, S65–S76.
- Olsen, K. B., 1994. *Simulation of three-dimensional wave propagation in the Salt Lake Basin*, Ph.D. Thesis, University of Utah, Salt Lake City, Utah, 157 pp.

- , 2000. Site amplification in the Los Angeles basin from threedimensional modeling of ground motion, *Bull. Seismol. Soc. Am.* **90**, S77–S94.
- Olsen, K. B., Archuleta, R. J., and Matarese, J. R., 1995. Three-dimensional simulation of a magnitude 7.75 earthquake on the San Andreas fault in southern California, *Science* **270**, 1628–1632.
- Olsen, K. B., Day, S. M., and Bradley, C. R., 2003. Estimation of Q for long-period (>2 s) waves in the Los Angeles Basin, *Bull. Seismol. Soc. Am.* **93**, 627–638.
- Olsen, K. B., Day, S. M., Minster, J. B., Cui, Y., Chourasia, A., Faerman, M., Moore, R., Maechling, P., and Jordan, T., 2006. Strong shaking in Los Angeles expected from southern San Andreas earthquake, *Geophys. Res. Lett.* **33**, L07305.
- Olsen, K. B., Day, S. M., Minster, J. B., Cui, Y., Chourasia, A., Okaya, D., Maechling, P., and Jordan, T., 2008. TeraShake2: Simulation of Mw7.7 earthquakes on the southern San Andreas fault with spontaneous rupture description, *Bull. Seismol. Soc. Am.* **98**, in press.
- Pitarka, A., 1999. 3D elastic finite-difference modeling of seismic motion using staggered grids with non-uniform spacing, *Bull. Seismol. Soc. Am.* **89**, 54–68.
- Pitarka, A., Irikura, K., Iwata, T., and Sekiguchi, H., 1998. Three dimensional simulation of the near fault ground motion for the 1995 Hyogoken Nanbu (Kobe), Japan earthquake, *Bull. Seismol. Soc. Am.* **88**, 428–440.
- Power, M., Chiou, B., Abrahamson, N., Bozorgnia, Y., Shantz, T., and Roblee, C., 2008. An overview of the NGA project, *Earthquake Spectra* **24**, 3–21.
- Somerville, P. G., Irikura, K., Graves, R. W., Sawada, S., Wald, D., Abrahamson, N., Iwasaki, Y., Kagawa, T., Smith, N., and Kowada, A., 1999. Characterizing crustal earthquake slip models for the prediction of strong ground motion, *Seismol. Res. Lett.* **70**, 59–80.
- Stewart, J. P., Choi, Y., Graves, R. W., and Shaw, J. H., 2005. Uncertainty of southern California basin depth parameters, *Bull. Seismol. Soc. Am.* **95**, 1988–1993.
- Suss, M. P., and Shaw, J. H., 2003. P-wave seismic velocity structure derived from sonic logs and industry reflection data in the Los Angeles basin, California, *J. Geophys. Res.* **108**, 2170, doi: 10.1029/2001JB001628.
- Trifunac, M. D., and Lee, V. W., 1978. *Dependence of the Fourier amplitude spectra of strong motion acceleration on the depth of sedimentary deposits*, University of Southern California, Department of Civil Engineering, Report No. CE 78-14, Los Angeles.
- Working Group on California Earthquake Probabilities, 1995. Seismic hazards in southern California: probable earthquakes, 1994 to 2024, *Bull. Seismol. Soc. Am.* **85**, 379–439.

(Received 1 July 2007; accepted 15 November 2007)